nature chemistry

ARTICLES

https://doi.org/10.1038/s41557-020-0495-3

Check for updates

Fast motion of molecular rotors in metal–organic framework struts at very low temperatures

Jacopo Perego[1], Silvia Bracco[1], Mattia Negroni[1], Charl X. Bezuidenhout[1], Giacomo Prando[2], Pietro Carretta[2], Angiolina Comotti[1]✉ and Piero Sozzani[1]✉

The solid state is typically not well suited to sustaining fast molecular motion, but in recent years a variety of molecular machines, switches and rotors have been successfully engineered within porous crystals and on surfaces. Here we show a fast-rotating molecular rotor within the bicyclopentane-dicarboxylate struts of a zinc-based metal–organic framework—the carboxylate groups anchored to the metal clusters act as an axle while the bicyclic unit is free to rotate. The three-fold bipyramidal symmetry of the rotator conflicts with the four-fold symmetry of the struts within the cubic crystal cell of the zinc metal–organic framework. This frustrates the formation of stable conformations, allowing for the continuous, unidirectional, hyperfast rotation of the bicyclic units with an energy barrier of 6.2 cal mol^{-1} and a high frequency persistent for several turns even at very low temperatures (10^{10} Hz below 2 K). Using zirconium instead of zinc led to a different metal cluster–carboxylate coordination arrangement in the resulting metal–organic framework, and much slower rotation of the bicyclic units.

Molecular dynamics phenomena are ubiquitous in nature, and often participate in the fundamental mechanisms of living systems[1–5]. Generally, fluid phases support such phenomena, while solid phases are universally considered to be least suitable to sustaining fast molecular motion. However, in solids, molecular moieties can be permanently set apart from each other, preventing mutual interactions and promoting unusual internal dynamics. This behaviour takes place in low-density solids, such as in metal–organic frameworks (MOFs), where non-interacting moving elements can be engineered[6–13]. Dynamics in solid phases can resemble those of liquid and gaseous phases, leading to unusual phenomena such as high thermal capacities, low surface friction and unexpected physical and chemical properties[14,15]. In recent years, incorporating molecular rotors, motors and switches in the solid state has been recognized as a major challenge; recently, the organization of rotating elements in the solid state or on surfaces has been shown to be an effective approach to translating their molecular dynamics into useful materials properties[16–21].

Our group and others have been working on integrating molecular rotors into porous materials, which combine a large free volume that promotes disentangled rotator revolution with the ability for chemical species to access—and intervene in—rotary mechanics[22–28]. Thus, rotor-containing porous materials provide a platform for the construction of ultra-fast reorienting elements in a robust framework. So far, a few rapid molecular rotors have been fabricated in porous frameworks by exploiting rotational axles pivoted on bonds with soft torsional barriers, such as sp^3–sp^2 and sp^2–sp bonds (Fig. 1a). This can be achieved by preventing the detrimental effects on the rotation caused by electronic conjugation between the rotator and stator and steric crowding between ligands (Fig. 1b)[29]. Indeed, rotors that had a high σ component on the pivotal bond or were adjacent to triple bonds achieved both the lowest energy barrier for rotation and the formation of multiple conformations corresponding to shallow energy minima[13,24]. Additionally, low rotor–rotor and rotor–framework interactions were minimized by exploiting the low packing density of the architectures.

Here we have synthesized two new MOFs, one with zinc and the other with zirconium as metal centres, both containing an aliphatic yet rigid building block bicyclopentane–dicarboxylate linker **1**—the bicyclic unit is the rotator, and the carboxylate group acts as a stator (Fig. 1c). In the zinc-based MOF, the cubic unit cell causes the planes of the two carboxylate units to arrange themselves perpendicularly (Fig. 1d). Hyperfast molecular rotor dynamics are provided by a combination of two things: the high torsional flexibility of the pivotal σ bond between the sp^3 carbons of the bicyclic unit and the carboxylate moieties, and the mismatch between the three-fold trigonal symmetry of the rotating unit and the four-fold carboxylate arrangement in the MOF (the zinc and zirconium MOFs are henceforth referred to as Zn-FTR and Zr-FTR, respectively, where FTR stands for frustrated trigonal-symmetry rotator). The torsional energy profiles on both sides of the rotator contribute out of phase, generating geometrical frustration with a virtually flat landscape (Fig. 1e). In Zr-FTR, the crystal structure induces an in-plane conformation of the two carboxylate units (Fig. 1f); thus, the rotator is surrounded by in-phase torsional barriers that sum to form a profile with six minima and with higher torsional barriers (Fig. 1g). The absence of either contact or long-range interactions among rotors in Zn-FTR reduces carbon–carbon torsional energy barriers to 6.2 cal mol^{-1}, which is lower than the thermal energy even at liquid helium temperature (RT = 8.0 cal mol^{-1} at 4 K). This behaviour was characterized by ^{1}H NMR; ^{1}H spin–lattice relaxation times (^{1}H T_1) were recorded down to 1.5 K. Measurements of ^{1}H T_1 at distinct magnetic fields (from 0.66 T to 7 T) show the characteristic field-independent behaviour expected in the fast-motional regime, where the dynamics are much faster than the nuclear precession frequency of 0.3 GHz at 7 T. Molecular dynamics simulations gave insight into the rotary mechanism and identified durable runs of hyperfast unidirectional continuous rotation rarely stopping in a single energy well.

Results and discussion

Structure of the MOF crystals. Zn-FTR was obtained by self-assembly at room temperature of the bicyclo[1.1.1]pentane-1,3-dicarboxylic

[1]Department of Materials Science, University of Milano Bicocca, Milan, Italy. [2]Department of Physics, University of Pavia, Pavia, Italy.
✉e-mail: angiolina.comotti@unimib.it; piero.sozzani@unimib.it

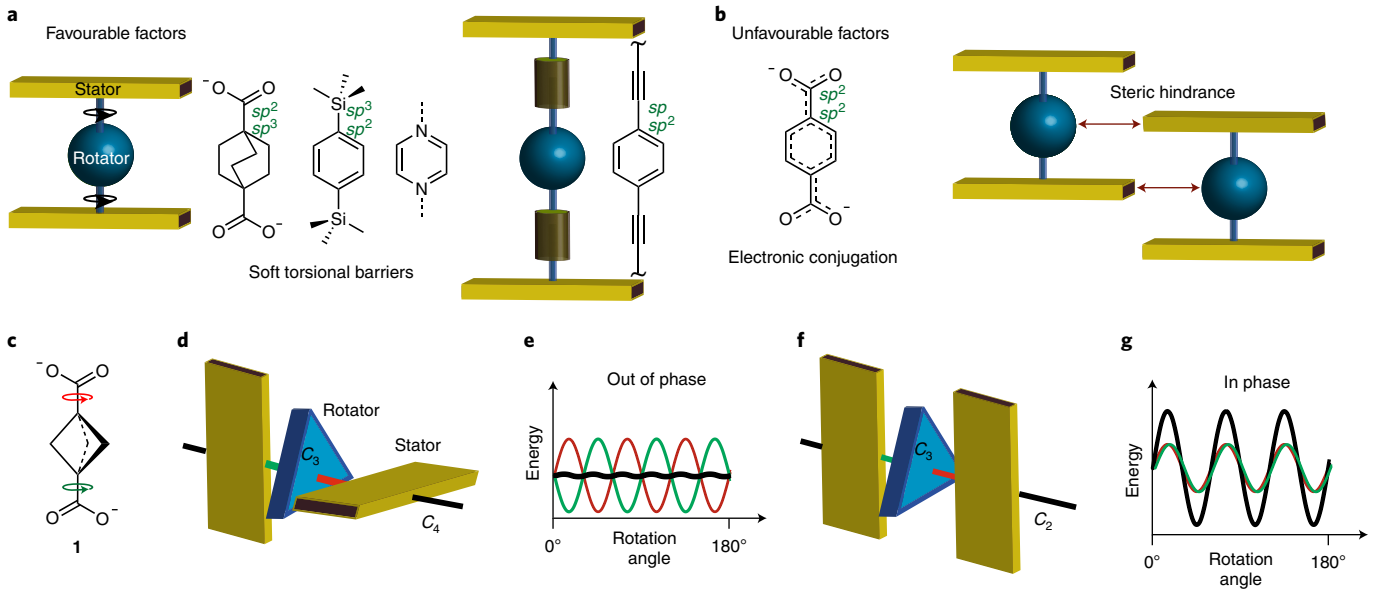

Fig. 1 | Factors influencing the molecular rotor dynamics, conformations of the rotator and stator in the ligand and the resulting energy profiles. **a**, Ligands containing molecular rotors with soft pivotal bonds (sp^3–sp^2 and sp^2–sp bonds) along the rotor axles. **b**, Electronic conjugation (sp^2–sp^2 bonds) within the ligand and intermolecular steric crowding negatively influencing rotor dynamics. **c**, Chemical structure of the bicyclo[1.1.1]pentane-1,3-dicarboxylate ligand **1**. **d**,**f**, Sketches of the ligand conformation highlighting the symmetry of both the rotator and stator. Dicarboxylate planes, as depicted by yellow parallelepipeds, are arranged perpendicular and parallel to each other. The blue triangles represent the bicyclic rotator. **e**,**g**, Individual torsional energy profiles about the bonds connecting the rotator to the stators (green and red lines) contributing out of phase to form an almost flat total energy profile (black line) (**e**) and in phase to increase energy barriers (**g**).

acid ligand with zinc ions in dimethylformamide (DMF), while Zr-FTR was obtained by a solvothermal synthesis modulated by formic acid to control the crystallization process. Porous crystalline architectures were obtained after gradual solvent exchange and activation under vacuum at 130 °C and 140 °C for Zn-FTR and Zr-FTR, respectively. Nanosized crystals of cubic and octahedral morphology were observed for Zn-FTR and Zr-FTR, respectively, as shown in SEM micrographs (Supplementary Figs. 4 and 5). The powder X-ray diffraction patterns were consistent with highly ordered crystalline porous materials, and the crystal structures were refined by the Rietveld method combined with molecular mechanics and plane-wave density functional theory (DFT) calculations (Supplementary Figs. 6 and 7). The crystal structure of Zn-FTR was also solved by single-crystal X-ray diffraction (Supplementary Figs. 9 and 10). Cubic crystal structures for Zn-FTR and Zr-FTR with space groups of *F*-43*c* and *F*32, respectively, were obtained (Fig. 2). The metal node in compound Zn-FTR comprises four zinc ions organized in tetrahedral clusters, coordinating six carboxylates bridging zinc pairs[30]. Comparatively, the use of zirconium dramatically changes the coordinative arrangement: 12-coordinated ligands spring from the nodes, forming a crowded arrangement[31,32]. The infrared spectra indicate that after coordination with zinc and zirconium ions, the C=O stretching bands of the carboxylate shift from 1,684 cm^{-1} in the free ligand to 1,609 cm^{-1} and 1,580 cm^{-1}, respectively (Supplementary Fig. 13). That there are three signals in the ^{13}C magic-angle-spinning (MAS) NMR spectra is consistent with the high symmetry of the unit cells (Supplementary Fig. 14).

Zn-FTR contains pores that can host spheres 10.6 Å in diameter, whereas Zr-FTR exhibits two smaller tetrahedral and octahedral cavities of 4.0 Å and 8.6 Å, respectively, as derived from the crystal structures (Fig. 2c,d). The porosity of the two MOFs was experimentally demonstrated by nitrogen adsorption isotherms at 77 K that displayed Langmuir type I profiles (Supplementary Figs. 16 and 17). The Zn-FTR material was found to have a surface area of 2,700 m^2 g^{-1} and a pore volume of 1.17 cm^3 g^{-1}, with a pore size

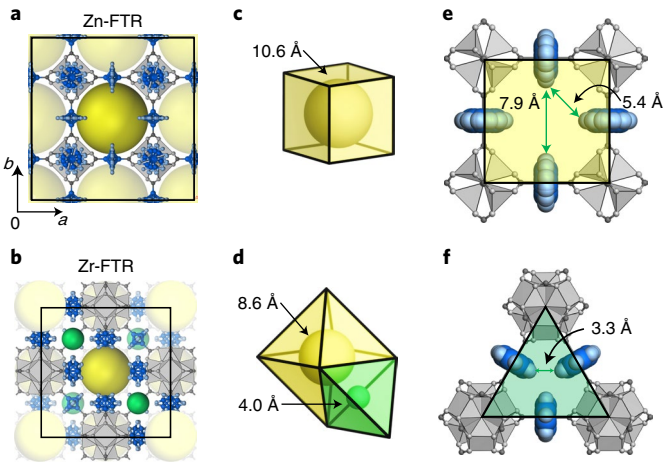

Fig. 2 | Crystal structure, cavity geometry and rotors in the frameworks. **a**,**b**, The crystal structures of Zn-FTR (**a**) and Zr-FTR (**b**) MOFs, obtained from the refinement of PXRD data, viewed along the *c*-axis. The metal-oxide nodes are shown in the polyhedron representation (metal nodes are shown in grey, carbons in light blue and hydrogens in white). **c**,**d**, The schematic geometries of the pores for both Zn-FTR (**c**) and Zr-FTR (**d**) as well as the largest spheres that can be accommodated within the pores. The diameters of the spheres, indicated in the figure, were based on considering the van der Waals radii of the host atoms. **e**,**f**, View showing the shortest distances between the rotor hydrogen atoms, as calculated from the centre of the nuclei, for Zn-FTR (**e**) and Zr-FTR (**f**).

distribution centred on 11.8 Å, in reasonable agreement with the pore sizes from the crystal structures. In the case of Zr-FTR, a surface area of 1,020 m^2 g^{-1} and a pore volume of 0.45 cm^3 g^{-1} were determined. The pore size distribution showed a peak centred on 8.5 Å

that corresponded to the diameter of the larger pores. The smaller pores are not detectable using nitrogen adsorption isotherms.

In the crystal structure of the Zn-FTR material, the three methylenes of the bicyclopentane rotator lie on a common plane, arranged as a wheel mounted on the main molecular axis of the ligand (Fig. 2e). The hydrogen atoms in each wheel in Zn-FTR are at distances of 7.9 Å and 5.4 Å from the next neighbouring rotor hydrogens. Consequently, they do not interfere with each other or with any other moiety in the rotary dynamics. The distances among the rotors are shorter in Zr-FTR (3.3 Å), but are still longer than the van der Waals contacts (Fig. 2f).

Rotor conformations and energy landscapes. A key point of the MOF crystal structure is that the carboxylate planes in Zn-FTR are set perpendicular to one another (crossed arrangement) while in Zr-FTR the carboxylate groups lie on a common plane (in-plane arrangement) (Fig. 3a,b). Both arrangements of the carboxylate end groups have been reported in the literature and depend on the nature of ligands and metal ions: for example, in MOF-5 the important contribution of the electronic conjugation with the aromatic ring determines the in-plane arrangement (see also Supplementary Fig. 21 and Supplementary Table 10). Ab initio conformational analysis of the bicyclopentane–dicarboxylate (**1**) showed that the crossed arrangement was more stable by 0.39 kcal mol^{-1} than the in-plane arrangement (Supplementary Fig. 18). However, the anchorage of the ligands to the metal nodes prevents conversion between arrangements in the structures. These arrangements have dramatic consequences for the energetics of the central rotator. The torsional conformations were investigated by MP2 potential energy scans. The conformations displayed minima every 60° (six-fold rotation axis) for the in-plane arrangement, while the energy minima occurred with a period of 30° (twelve-fold rotation axis) for the crossed arrangement (Fig. 3c,d). In both cases, the energy barriers, as calculated by MP2/6-311+G(d), are of a few calories per mole. The energy barrier of the in-plane conformation was 50 cal mol^{-1}, while in the crossed arrangement it was found to be lower than a few calories per mol and comparable to the thermal agitation at 0.5 K (Fig. 3e), showing the extremely high torsional flexibility of the rotator, comparable to methyl rotation flexibility[33–36].

To rationalize the energy profiles in the two distinct conformations and how the nearly degenerate states occur in the crossed arrangement, one must consider that the rotor interacts periodically with both adjacent carboxylates on opposite sides of the rotor plane—that is, the plane perpendicular to the main axis of the ligand. The energy profile for the interaction of the rotor with each carboxylate generates six minima, consistent with the combination of the two-fold and three-fold symmetries of the carboxylates and the rotator, respectively. The total energy potential is then a summation of the two potentials generated by the rotation of the bicyclic moiety with respect to the two planes of the carboxylate groups on either side (Fig. 3f,g). In the in-plane conformation, the two potentials are in phase ('constructive interference'), so that the profile is retained and intensified. By contrast, in the crossed conformation, the two periodic functions are shifted by half a period and are out of phase; thus the proper mismatch of the added potentials produces the observed 'destructive interference', and the rotor is frustrated in its tendency to fall into deep minima.

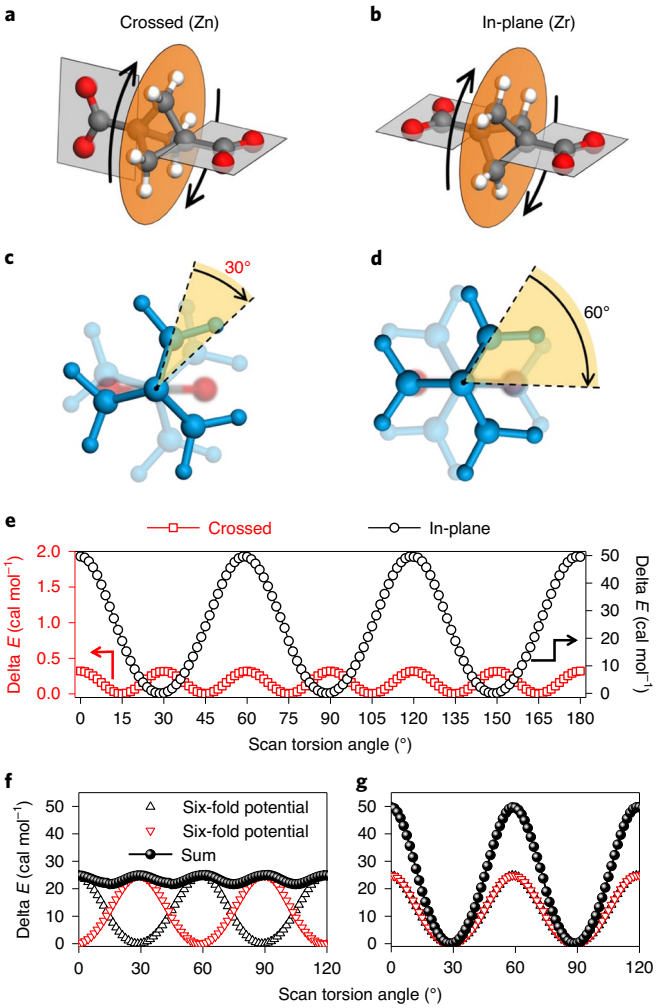

Fig. 3 | Crossed (Zn) and in-plane (Zr) conformations with torsional energy profiles of the ligands. a,**b**, Rotor minimum conformations for crossed and in-plane arrangements as in Zn-FTR and Zr-FTR, respectively. **c**,**d**, Conformational minima for the crossed and in-plane arrangements occurring by rotations of 30° and 60°, respectively. **e**, An overlay of the crossed (red squares) and in-plane (black circles) potential energy surface scans plotted from 0° to 180° with separate *y*-axis scales (crossed on the left in red and in-plane on the right in black). **f**,**g**, Six-fold torsional potential of the rotator about the C–C bond with each carboxylate moiety (black and red triangles) for the out-of-phase and in-phase conformations, respectively. The mathematical summations of two six-fold potentials for the out-of-phase and in-phase conformations are represented as black spheres. In the case of the out-of-phase summation, the mismatch between the potentials led to a substantial compensation (crossed conformation, 12 minima); in the case of in-plane summation, the profile is retained and intensified (in-plane conformation, 6 minima).

Rotor dynamics. An effective tool for providing evidence of dynamics in crystalline matter is variable-temperature solid-state NMR spectroscopy. The ^{13}C NMR spectra of Zn-FTR, recorded under static conditions that would potentially highlight the anisotropic profile, exhibited pseudo-isotropic signals for methylenes, both at room temperature and down to 163 K. The spectra of Zn-FTR and Zr-FTR showed narrow lines with widths of 1.4 ppm and 2 ppm, respectively, depicting a rotary revolution that is fast enough to average out chemical shift anisotropy (CSA) (Fig. 4a, red lines)[37]. For comparison, Fig. 4a shows the full CSA profile determined by ab initio GIAO calculations (dashed black line), which is consistent with the CSA profile of the reference compound, bicyclopentane hydrocarbon. The mixing of the principal tensor components in the *x*–*y* plane orthogonal to the rotor axis (σ_{xx} = 44 ppm and σ_{yy} = 60 ppm, Fig. 4b) produces an average value of 52 ppm, which is equal to the σ_{zz} component. The latter is unaffected by rotator reorientation, being parallel to the rotation axis. This restriction of CSA to isotropic lines in the solid state is of the same order of magnitude as that in globular molecules, such as adamantane and fullerene,

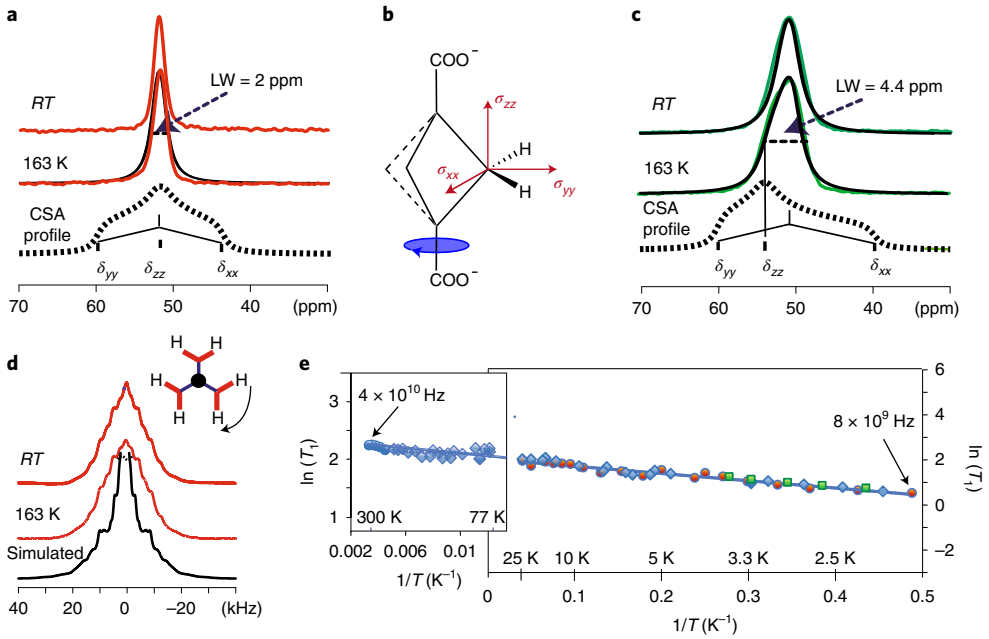

Fig. 4 | Solid-state NMR spectra and ^{1}H T_1 spin–lattice relaxation times of the molecular rotor in the MOFs recorded at various magnetic fields. **a**,**c**, Cross-polarization MAS ^{13}C NMR spectra of Zn-FTR (**a**, red) and Zr-FTR (**c**, green) at room temperature and 163 K and restricted CSA profiles (black) calculated by considering fast rotation of CH_2 moieties about their main axes. Line widths (LWs) are shown as long-dashed lines. Full theoretical CSA profiles are shown as dashed lines. **b**, Chemical structure of bicyclopentane-dicarboxylate (**1**) and the main components of the ^{13}C CSA tensor. **d**, Solid-state ^{1}H NMR spectrum of Zn-FTR collected under static conditions at room temperature and at 163 K (red) and the simulated pattern (black) obtained from the dipolar couplings among a cluster of six hydrogens, as in an isolated bicyclic-based molecule. **e**, ln ^{1}H T_1 relaxation times versus the reciprocal of temperature in the temperature range from 1.5 K to 300 K. The T_1 relaxation times were measured at 7.04 T (blue circles), 1.66 T (green squares), 1.0 T (blue diamonds) and 0.66 T (orange circles).

which display line-widths of 5 ppm at 298 K and of 2.4 ppm at 190 K, respectively—although in these cases, phase transitions prevent fast dynamics at lower temperatures[38,39]. For comparison, at 163 K the sterically hindered Zr-FTR shows a residual CSA profile and a 4.4 ppm line-width, with a prominent peak corresponding to the mixing of σ_{xx} and σ_{yy} and a lateral signal for the σ_{zz} component (Fig. 4c, green line). The identification of a separate σ_{zz} component that is not mixed with the remaining tensors clearly highlights the axial symmetry of the rotary trajectories.

Solid-state ^{1}H NMR spectra of Zn-FTR displayed methylene signals with a 10 kHz line-width (Fig. 4d), which appear markedly modulated by through-space homonuclear dipolar couplings even at 2 K. The unusual ^{1}H NMR spectrum patterning was successfully simulated by considering the orientation and distance dependence of the dipole–dipole interactions in the six-spin cluster of an individual rotor under magnetic and molecular isolation. The spectra are essentially a combination of 'Pake' patterns (characteristic lineshapes from dipolar couplings) containing the anisotropic information and dynamic averaging among hydrogens in the rotator plane (Supplementary Fig. 23). A similar six-nuclei modulated spectrum has only been investigated in fast-spinning benzene within a graphite layer[40]. An orbital trajectory of hydrogen nuclei, perpendicular to the rotor main axis in the fast motion limit ($>10^8$ Hz), was demonstrated by the overall line-shape restriction of the full 'static' powder pattern to be half of its width. Furthermore, taking into account hydrogen–hydrogen dipolar interactions in the crystal cell, we evaluated the second moment and demonstrated that 98% of the effective interactions occur within the six methylene hydrogens of each rotator (Fig. 4d and Supplementary Fig. 24)[41]. Importantly, from this evaluation it was possible to calculate the relaxation constant C of 5.8×10^9 s^{-2} (proportional to the mean square amplitude of the fluctuating field at the nuclei), which is used below to establish the correlation times from NMR spin–lattice relaxation times.

Solid-state NMR relaxation times enable the exploration of material dynamics and, when collected at various resonance frequencies, give access to reorientation rates over several orders of magnitude. The ^{1}H T_1 of the bicyclopentane methylenes in Zn-FTR were measured from 298 K down to 1.5 K at a few distinct main magnetic fields B_0 equal to 7.04 T, 1.66 T, 1.00 T and 0.66 T (Fig. 4e; 70 points were collected). The relaxation times were plotted as $\ln(T_1)$ versus $1/T$ and fitted by the universal master curve, according to the Kubo–Tomita theory[42]. The plot exhibits a field-independent linear decrease with inverse temperature and a constant slope over the entire range (Fig. 4e; the 77–298 K range is expanded for clarity). This indicates that the relaxation times are determined by dynamics much faster than the nuclear Larmor frequency, even at extremely low temperatures. The value for the rotation barrier was as low as 6.2 cal mol^{-1} (26 J mol^{-1}) for Zn-FTR. Muon spin relaxation experiments support the extremely low energy barrier (Supplementary Section 2.17). The very low activation energy value supports the almost negligible energy barriers for rotation in this molecular rotor. By taking into account the previously determined relaxation constant C, the correlation times can be established for each temperature. Importantly, the correlation time at 'infinite' temperature, τ_0, of 4×10^{-12} s is consistent with the theoretical value of 4.2×10^{-12} s, as derived from the potential of the rotating system of 42 mass units (three carbons plus six hydrogens, moment of inertia of 8.23×10^{-22} kg m^2 mol^{-1}) (Supplementary Section 1.2)[43]. This adds further support to our assignment that the bicyclic 'molecular wheels' in Zn-FTR operate as individual rotating entities, independently from each other.

Hyperfast rotary motion of $k=37$ GHz (the reciprocal of the correlation time $1/\tau_c=2.3\times10^{11}$ s^{-1}) at room temperature was established and was still in the gigahertz regime ($k=7.9\times10^9$ Hz

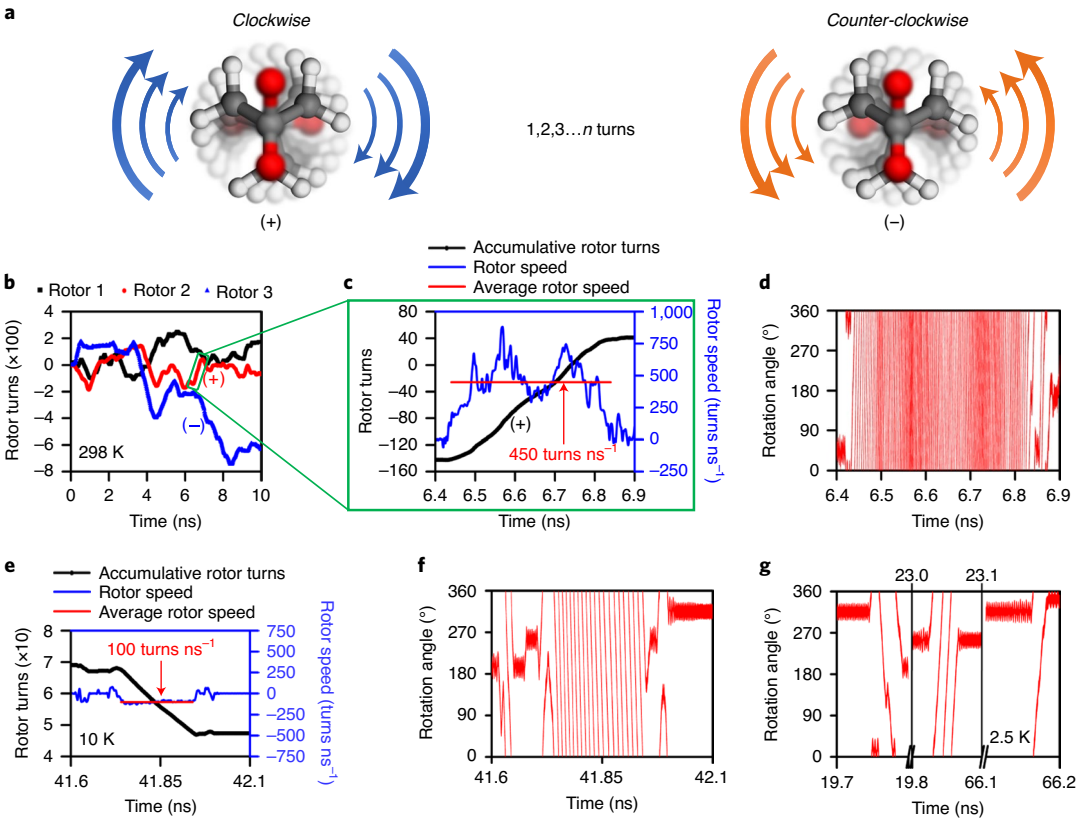

Fig. 5 | Molecular dynamics results for Zn-FTR calculated at various temperatures. a, An illustration of clockwise and counter-clockwise rotation of the bicyclic rotating moiety showing the multiple turns performed in a single direction (carbons shown in grey and oxygens in red). **b**, The time evolution of the cumulative torsion angular displacement at 298 K, reported as number of turns, starting from an arbitrary zero configuration of three selected rotators; clockwise or counter-clockwise rotation is indicated by positive or negative signs. **c**, An enlarged section (0.5 ns) of the 298 K dynamics simulation highlighting a continuous unidirectional rotation for 225 turns (black line) and the associated angular speed (blue line) and average speed (red line) expressed as number of turns per nanosecond. **d**, The 298 K rotator angular displacement represented on a 0–360° scale for the 0.5 ns time window. **e**, A section of the 10 K dynamics simulation highlighting a continuous unidirectional movement (black line), the associated angular speed (blue line) and the average speed (red line) during a 0.5 ns time period. **f**, The 10 K rotator angular displacement represented on a 0–360° scale. **g**, The 2.5 K rotator angular displacement represented on a 0–360° scale showing different time windows of the dynamics simulation.

and $1/\tau_c = 5.0 \times 10^{10}\,s^{-1}$) at temperatures as low as 2 K. Such a low energy barrier for rotary dynamics allows $k = 7.3 \times 10^7$ Hz ($1/\tau_c = 4.5 \times 10^8\,s^{-1}$) rotation to occur at a temperature as low as 0.5 K. To the best of our knowledge, fast molecular rotors in organic matter have not been observed at liquid helium temperature and below, because the energy barrier in such rotors is well above the thermal energy and the rotation frequency is reduced to less than 1 Hz (refs. [13,24]). Unlike other examples reported in the literature, 'unrestricted' motion for the entire temperature range (2–300 K) was achieved with a relatively large inertial mass. No evidence for slope change at low temperature, which could indicate a regime of tunnelling[43,44], is observed in the spin–lattice relaxation times. The dynamics shown here are approaching the fastest rotational speed observed at low temperature for organic moieties, such as methyl groups, in the solid phase—and even in the gas phase[33,45]. The low rotation barrier determined here suggests that the rotor symmetry frustration obtained in the MOF host ensures high mechanical flexibility.

Modulation of rotor speed. Observing the same bicyclopentane rotor in the sterically hindered Zr-FTR structure, which imposes a different symmetry and density, probes the effect of the crystal environment on the rotor freedom. In Zr-FTR, a higher energy barrier of 400 cal mol^{-1} for rotation (Supplementary Fig. 32) and shorter distances between the rotors (3.3 Å) are observed.

In addition, modulation of the rotation speed was achieved under chemical stimulus in porous Zn-FTR by the introduction of gaseous I_2, which interacts with the rotors accessible through the open pores. Indeed, in the presence of I_2 molecules diffusing spontaneously into the porous crystals at 27 mbar vapour pressure and 293 K, the rotary speed was drastically reduced. It was still, however, in the fast motion regime: the energy barrier increased to 1,000 cal mol^{-1}, that is, three orders of magnitude larger than the empty (guest-free) matrix (Supplementary Fig. 32). This increase in activation energy from a negligible value was ascribed to a 'weak' favourable interaction of the C–H peripheral methylenes of the rotor wheel with the I_2 molecules in the pores. This modulation of the rotation speed served to probe the sensitivity of the material to any minimal perturbation, which could be useful as a prompt and reversible detector.

Molecular dynamics simulations. Molecular dynamics simulations helped provide a deeper insight into the functioning of the molecular rotors (Fig. 5). The rotor dynamics were determined by analysing the evolution of the rotatory torsion angles with respect to time for three rotators selected as representative of the entire population for each compound (Supplementary Fig. 36). In both compounds the rotor axis oscillations (nutation) are not larger than 3° at any temperature (Supplementary Fig. 33). The robustness of the double anchorage (the carboxylate groups on either side of the

bicyclic rotating moiety) firmly supports the axle to the framework, unlike a methyl rotor, which is mono-dentate and is thus pivoted on only one side[35,45]. The cumulative angular displacement of the rotors at room temperature, shown in number of turns, is depicted in Fig. 5b for the three selected rotators in Zn-FTR. Clockwise or counter-clockwise rotation can be differentiated by positive or negative angular displacement, respectively.

The rotator neither resides in a single energy minimum, oscillating therein, nor moves stepwise by jumping from one minimum to the next. Conversely, a multiple-turn displacement, overflying a large number of energy minima (up to 4,000 minima; 12 minima are equal to 1 turn), was observed. The molecular wheel appears to spin freely and performs a diffusional motion, overriding negligible minima for up to 500 continuous unidirectional revolutions in either clockwise or counter-clockwise directions, depicting a waving behaviour as shown in Fig. 5b,c. By representing the rotation angles explored by an individual rotator in a 0–360° scale against time, the signature of the continuous motion becomes imprinted as parallel noiseless lines (Fig. 5d). Chaotic thermal energy is higher than the activation energy for rotation, but, at the same time, the 42-dalton rotational mass of the rotator is high enough to ensure the unusual conservation of rotational momentum for a certain period of time. Indeed, such inertial behaviour, combined with a flat energy profile, allows for continuous unidirectional motion that lasts for as long as 0.5 ns at room temperature. The rotary speed, sampled as the average slope (the derivative of the cumulative angle versus time) over several turns in a lasting continuous rotation, was as fast as 4.5×10^{11} Hz (Fig. 5b,c). This value is in very good agreement with the correlation time τ_0 of 4.3×10^{-12} s measured experimentally by NMR relaxation and Kubo–Tomita analysis.

At low temperature, the rotators possess lower thermal energy and can occasionally be trapped in potential energy wells (Fig. 5e). The rapid, intermittent, stop-and-go behaviour and the persistence at low temperatures of hyperfast rotation manifested in continuous unidirectional motion (Fig. 5f,g), suggesting that the rotator explores energetic states higher than the tiny energy barrier, even at 2.5 K. The direction can be easily recognized in each free-rotation packet by the positive or negative inclination of the parallel lines. By comparison, Zr-FTR, characterized by a higher barrier, shows conventional frequently occurring jumps from one energy well to the next (Supplementary Figs. 41, 42, and 48).

Conclusions

We have realized a fast molecular rotor in the solid state whose rotation speed approaches that of unhindered rotations in organic moieties and is shown to be faster than methyl rotation even at very low temperatures (2 K). The bicyclopentane rotors were hosted within the struts of a low-density porous crystalline MOF and energetically decoupled from their surroundings. The rotors, isolated from one another in the high-symmetry structure, showed a negligible torsional barrier to rotation. A key point was the unusual crossed conformation adopted by the carboxylates around the pivotal bond on the rotor axle, generating a four-fold symmetry that does not match the three-fold rotation symmetry of the rotator. This produced geometrical frustration and, for a full turn, 12 very shallow wells along the circular trajectory.

This behaviour is the result of the continuous unhindered molecular wheel rotation for several turns, rather than the jumping motion usually observed for barrier-restricted rotations. The present system demonstrates the existence of dynamic materials under very low temperatures, perhaps suggesting future investigations into regular arrays of rotary motors and rotors showing enhanced performance under low thermal-perturbation conditions. Molecular motors and switches must compete with thermal noise, which interferes with their coherent functioning. Temperature reduction to the lowest limit can be envisaged to minimize the disturbance of thermal energy and perform coherent tasks. However, this reduction generally hinders molecular dynamics. Instead, fast molecular motors and switches can extend their working range to low temperatures, provided that the torsional barriers are sufficiently lower than thermal energy.

Online content

Any methods, additional references, Nature Research reporting summaries, source data, extended data, supplementary information, acknowledgements, peer review information; details of author contributions and competing interests; and statements of data and code availability are available at https://doi.org/10.1038/s41557-020-0495-3.

Received: 5 August 2019; Accepted: 27 May 2020;
Published online: 6 July 2020

References

1. Saibil, H. Chaperone machines for protein folding, unfolding and disaggregation. *Nat. Rev. Mol. Cell Biol.* **14**, 630–642 (2013).
2. Kinbara, K. & Aida, T. Towards intelligent molecular machines: Directed motions of biological and artificial molecules and assemblies. *Chem. Rev.* **105**, 1377–1400 (2005).
3. Olesen, C. et al. The structural basis of calcium transport by the calcium pump. *Nature* **450**, 1036–1042 (2007).
4. Howard, J., Hudspeth, A. J. & Vale, R. D. Movement of microtubules by single kinesin molecules. *Nature* **342**, 154–158 (1989).
5. Preben Morth, J. et al. A structural overview of the plasma membrane Na^+,K^+-ATPase and H^+-ATPase ion pumps. *Nat. Rev. Mol. Cell Biol.* **12**, 60–70 (2011).
6. Vogelsberg, C. S. & Garcia-Garibay, M. A. Crystalline molecular machines: function, phase order, dimensionality, and composition. *Chem. Soc. Rev.* **41**, 1892–1910 (2012).
7. Bracco, S., Comotti, A. & Sozzani, P. Molecular rotors built in porous materials. *Acc. Chem. Res.* **49**, 1701–1710 (2016).
8. Danowski, W. et al. Unidirectional rotary motion in a metal-organic framework. *Nat. Nanotechnol.* **488**, 488–494 (2019).
9. Deng, H., Olson, M. A., Stoddart, J. F. & Yaghi, O. M. Robust dynamics. *Nat. Chem.* **2**, 439–443 (2010).
10. Zhu, K., O'Keefe, C. A., Vukotic, V. N., Schurko, R. W. & Loeb, S. J. A molecular shuttle that operates inside a metal-organic framework. *Nat. Chem.* **7**, 514–519 (2015).
11. Kobr, L. et al. Inclusion compound based approach to arrays of artificial dipolar molecular rotors. A surface inclusion. *J. Am. Chem. Soc.* **134**, 10122–10131 (2012).
12. Inukai, M. et al. Control of molecular rotor rotational frequencies in porous coordination polymers using a solid-solution approach. *J. Am. Chem. Soc.* **137**, 12183–12186 (2015).
13. Vogelsberg, C. S. et al. Ultrafast rotation in an amphidynamic crystalline metal organic framework. *Proc. Natl Acad. Sci. USA* **114**, 13613–13618 (2017).
14. Michl, J., Charles, E. & Sykes, H. Molecular rotors and motors: recent advances and future challenges. *ACS Nano* **3**, 1042–1048 (2009).
15. Prokop, A., Vacek, J. & Michl, J. Friction in carborane-based molecular rotors driven by gas flow or electric field: classical molecular dynamics. *ACS Nano* **6**, 1901–1914 (2012).
16. Coskun, A., Banaszak, M., Astumian, R. D., Stoddart, J. F. & Grzybowski, B. A. Great expectations: can artificial molecular machines deliver on their promise? *Chem. Soc. Rev.* **41**, 19–30 (2012).
17. Steuerman, D. W. et al. Molecular-mechanical switch-based solid-state electrochromic devices. *Angew. Chem. Int. Ed.* **43**, 6486–6491 (2004).
18. Collier, C. P. et al. A [2]catenane-based solid state electronically reconfigurable switch. *Science* **289**, 1172–1175 (2000).
19. Kaleta, J. et al. Surface inclusion of unidirectional molecular motors in hexagonal tris(o-phenylene) cyclotriphosphazene. *J. Am. Chem. Soc.* **139**, 10486–10498 (2017).
20. Jiang, X. et al. Crystal fluidity reflected by fast rotational motion at the core, branches, and peripheral aromatic groups of a dendrimeric molecular rotor. *J. Am. Chem. Soc.* **138**, 4650–4656 (2016).
21. Comotti, A., Bracco, S., Ben, T., Qiu, S. & Sozzani, P. Molecular rotors in porous organic frameworks. *Angew. Chem. Int. Ed.* **53**, 1043–1047 (2014).
22. Comotti, A. et al. & . Engineering switchable rotors in molecular crystals with open porosity. *J. Am. Chem. Soc.* **136**, 618–621 (2014).
23. Bracco, S. et al. CO_2 regulates molecular rotor dynamics in porous materials. *Chem. Commun.* **53**, 7776–7779 (2017).
24. Bracco, S. et al. Ultrafast molecular rotors and their CO_2 tuning in MOFs with rod-like ligands. *Chem. Eur. J.* **23**, 11210–11215 (2017).

25. Bracco, S. et al. & . Dipolar rotors orderly aligned in mesoporous fluorinated organosilica architectures. *Angew. Chem. Int. Ed.* **54**, 4773–4777 (2015).
26. Horike, S. et al. & . Dynamic motion of building blocks in porous coordination polymers. *Angew. Chem. Int. Ed.* **45**, 7226–7230 (2006).
27. Zhu, K., Vukotic, V. N., Okeefe, C. A., Schurko, R. W. & Loeb, S. J. Metal–organic frameworks with mechanically interlocked pillars: controlling ring dynamics in the solid-state via a reversible phase change. *J. Am. Chem. Soc.* **136**, 7403–7409 (2014).
28. Elsaidi, S. K. et al. Effect of ring rotation upon gas adsorption in SIFSIX-3-M (M = Fe, Ni) pillared square grid networks. *Chem. Sci.* **8**, 2373–2380 (2017).
29. Gonzalez-Nelson, A., Coudert, F. X. & van der Veen, M. Rotational dynamics of linkers in metal–organic frameworks. *Nanomaterials* **9**, 330–366 (2019).
30. Li, H., Eddaoudi, M., O'Keeffe, M. & Yaghi, O. M. Design and synthesis of an exceptionally stable and highly porous metal–organic framework. *Nature* **402**, 276–279 (1999).
31. Cavka, J. H. et al. & . A new zirconium inorganic building brick forming metal–organic frameworks with exceptional stability. *J. Am. Chem. Soc.* **130**, 13850–13851 (2008).
32. Yuan, S., Qin, J.-S., Lollar, C. T. & Zhou, H.-C. Stable metal–organic frameworks with group 4 metals: Current status and trends. *ACS Cent. Sci.* **4**, 440–450 (2018).
33. Owen, N. L. in *Internal Rotation in Molecules* (ed. Orville-Thomas, W. J.) Ch. 6 (Wiley, 1974).
34. Nakagawa, J. & Hayashi, M. Microwave spectrum and internal rotation of 2-butyne-1, 1, 1-d_3(dimethylacetylene), $CH_3C{\equiv}CCD_3$. *J. Chem. Phys.* **80**, 5922–5925 (1984).
35. Ilyushin, V. et al. Almost free methyl top internal rotation: Rotational spectrum of 2-butynoic acid. *J. Mol Spectrosc.* **267**, 186–190 (2011).
36. Hensel, K. D. & Gerry, M. C. L. Microwave spectrum of tetrolyl fluoride. *J. Chem. Soc. Faraday Trans.* **90**, 3023–3027 (1994).
37. Facelli, J. C. et al. & . Low-temperature carbon-13 magnetic resonance in solids. 5. Chemical shielding anisotropy of the $^{13}CH_2$ group. *J. Am. Chem. Soc.* **107**, 6749–6754 (1985).
38. Gil, A. M. & Alberti, E. The effect of magic angle spinning on proton spin–lattice relaxation times in some organic solids. *Solid State Nucl. Magn. Reson.* **11**, 203–209 (1998).
39. Ticko, R. et al. & . Molecular dynamics and the phase transition in solid C_{60}. *Phys. Rev. Lett.* **67**, 1886–1889 (1991).
40. Panich, A. M. & Panich, E. A. NMR lineshape of a six-spin system with dipole-dipole interactions. Application to benzene. *J. Magn. Res. Series A* **116**, 113–116 (1995).
41. Goc, R. Computer calculation of the Van Vleck second moment for materials with internal rotation of spin groups. *Comput. Phys. Commun.* **162**, 102–112 (2004).
42. Kubo, R. & Tomita, K. A general theory of magnetic resonance adsorption. *J. Phys. Soc. Jpn* **9**, 888–919 (1954).
43. Koksal, F. & Rossler, E. Spin–lattice relaxation by tunneling motions of methyl groups in some organic compounds. *Solid State Commun.* **44**, 233–235 (1982).
44. Layanowicz, L. Spin–lattice NMR relaxation and second moment of NMR line in solids containing CH_3 groups. *Concepts Magn. Reson.* **44A**, 214–225 (2015).
45. Eibl, K., Kannengießer, R., Stahl, W., Nguyen, H. V. L. & Kleiner, I. Low barrier methyl rotation in 3-pentyn-1-ol as observed by microwave spectroscopy. *Molecular Phys.* **114**, 3483–3489 (2016).

Methods

Synthesis of Zn-FTR. A solution of $Zn(CH_3COO)_2{\cdot}2H_2O$ (197.56 mg; 0.90 mmol) in dry N,N-DMF (3 ml) was added dropwise to a solution of 1,3-bicyclo[1.1.1] pentanedicarboxylic acid (**1**) (46.84 mg; 0.30 mmol) in dry N,N-DMF (3 ml) over a period of 5 min at room temperature under stirring. The mixture was additionally stirred for 30 min and then left under static conditions for 16 h. The white precipitate was centrifuged and the supernatant replaced by fresh dry DMF four times (4 × 5 ml). The solvent was exchanged and the sample was soaked in dry dichloromethane for 2 d, replacing the solvent two times a day. The material was activated in high vacuum at room temperature for 8 h and then at 130 °C overnight. The sample is stable under inert atmosphere (for example, nitrogen atmosphere), and at low relative humidity (RH ≤ 30%) it is stable for several hours.

Synthesis of Zr-FTR. $ZrCl_4$ (144.6 mg; 0.62 mmol) and 1,3-bicyclo[1.1.1] pentanedicarboxylic acid (**1**) (290.4 mg; 1.86 mmol) were dispersed in a mixture of dry DMF (24 ml) and formic acid (456 µl; 12 mmol) in a 100 ml glass vial, and the mixture was sonicated for 1 min at room temperature and then heated at 120 °C for 22 h. Then, the vial was taken out of the oven and cooled at room temperature. The white solid was filtered on a 0.2 µm PTFE filter and washed with DMF (100 ml) and methanol (100 ml). The resulting powder was activated in high vacuum, first at room temperature, and then at 140 °C overnight.

I_2 loading in Zn-FTR. A sample of Zn-FTR (57 mg) was placed inside a 2.5 ml glass vial, which was inserted in a Schlenk tube and treated at 130 °C under high vacuum overnight. After cooling to room temperature, the sample was exposed to I_2 vapours for 72 h in static vacuum conditions. Finally, the I_2 source was disconnected and the I_2 loaded sample (I_2@Zn-FTR) was analysed using infrared spectroscopy, powder X-ray diffraction (PXRD) and solid-state NMR.

Solution ^{1}H NMR. The ^{1}H NMR spectra were recorded on a 500 MHz Bruker instrument. Chemical shifts are reported in ppm.

Infrared spectroscopy. Infrared spectra were measured with a Jasco FT/IR 4100 equipped with an ATR PRO450-S module. The samples were evacuated under high vacuum at 130 °C (Zn-FTR) and 140 °C (Zr-FTR) before analysis to ensure the complete removal of adsorbed water vapour and guest species. Spectra were collected in transmission mode between 600 cm^{-1} and 4,000 cm^{-1} with a resolution of 2.0 cm^{-1}.

Micro-infrared (Micro-FTIR) spectra were measured on a Nicolet iN10 Infrared Microscope (Thermo Fisher Scientific) equipped with a liquid nitrogen cooled detector, working in reflection mode. The sample was degassed at 140 °C for 12 h before the measurement and quickly deposited on a gold substrate for analysis. Spectra were collected with a resolution of 4 cm^{-1} between 600 cm^{-1} and 4,000 cm^{-1}.

Thermogravimetric analysis. Thermogravimetric analyses were performed using a Mettler Toledo Star System 1 equipped with a GC10 gas controller. The experiments were conducted in air, applying a ramp from 25 °C to 800 °C and a scan rate of 10 °C min^{-1}.

Scanning electron microscopy. Scanning electron microscope images were collected using a Zeiss Gemini 500 scanning electron microscope operating at 5 kV. Samples were cast on a silicon slide from 2-propanol or THF dispersion.

Adsorption isotherms. Nitrogen adsorption isotherms at 77 K were collected up to 1 bar using a Micromeritics ASAP2020 HD analyser. Samples were previously outgassed overnight at 130 °C (Zn-FTR) and 140 °C (Zr-FTR) to remove all the adsorbed species. Low temperature (77 K) nitrogen adsorption Langmuir and BET isotherms were fitted and surface areas were calculated in the range from 0.015 p/p° to 0.1 p/p°. Pore size distributions were calculated according to DFT.

PXRD and structure refinement. PXRD measurements were accomplished with a Rigaku powder diffractometer using Cu-Kα radiation, 40 kV, 15 mA over a range for 2θ of 4.0–70.0° with a step size of 0.02° and a scan speed of 0.3° s^{-1}. Indexing and Rietveld refinement were performed using the TOPAS-Academic-64 V6 software package[46,47]. The initial input structure used for the PXRD refinement was generated using the CASTEP code (DFT) within the Biovia Materials Studio software package. The DFT optimizations had the unit cell restrained to the PXRD indexed cell parameters while all the molecules could be optimized. Optimizations were performed using the GGA PBE functional with Grimme's DFT-D dispersion correction; thresholds for geometry optimization and SCF convergence were chosen to be 2×10^{-6} eV. The unit-cell parameters were kept fixed while all the atoms were allowed to optimize. The hydrogen atoms of the DFT-optimized structure were normalized to neutron diffraction distances using the 'normalized' option in the Mercury V 3.9 software package[48]. The unit-cell parameters were kept fixed throughout the refinement process. A DFT potential energy scan reveals a 30° (four-fold rotation) and 60° (two-fold rotation) rotational disorder for the Zn-FTR and Zr-FTR rotors, respectively. Applying these disordered models to the structures yields a symmetry of *F*-43*c* for Zn-FTR and *F*32 for Zr-FTR. Further Rietveld refinements were performed using these space groups and the disordered models. The background was fitted and refined using a Chebyshev polynomial with 20 coefficients in the range of the PXRD trace, with a range for 2θ of 5–60° for Zn-FTR and 5–70° for Zr-FTR and the application of baseline shift refinement. Other corrections include: Specimen Displacement, Divergence Sample Length, Absorption with Sample Thickness Shape Intensity, and Specimen Tilt. The peaks were fitted using a modified Thompson–Cox–Hastings pseudo-Voigt 'TCHZ' profile. Preferred orientation was considered using a combination of March-Dollase ((100), (010), (001), (110), (011), (101)) and an eighth order spherical harmonics refinement.

Single-crystal XRD and crystal structure refinement. Single crystals of Zn-FTR (CCDC number 1994502) were synthesized under solvothermal conditions. $Zn(NO_3)_2{\cdot}6H_2O$ (148.8 mg; 0.5 mmol) and 1,3-bicyclo[1.1.1]pentanedicarboxylic acid (31.2 mg; 0.2 mmol) were dissolved in dry N,N-DMF (30 ml) in a 100 ml vial. The solution was heated at 120 °C for 24 h and allowed to cool at room temperature. A suitable prismatic crystal was mounted on a Bruker D8 PhotonII diffractometer and the data collection was performed at 150 K. Data reduction was performed using SAINT (Bruker software, 2012) and the absorption correction was applied with the program SADABS[49]. Using Olex2[50], the structure was solved with the ShelXS[51] program using direct methods and it was refined with the ShelXL[52] program using least squares minimization.

Crystal structure determination of Zn-FTR (CCDC 1994502). Crystal data for $C_6O_{3.25}ZnH$ ($M = 189.43$ g mol^{-1}): cubic, space group *P*-43*m* (no. 215), the crystallographic *a*-axis = 11.949 Å, unit cell volume $V = 1{,}706.2$ Å^3, number of formula units in the unit cell $Z = 4$, $T = 150.0$ K, linear absorption coefficient $\mu(MoK\alpha) = 1.415$ mm^{-1}, calculated density of the unit cell $D_{calc} = 0.741$ g cm^{-3}, 44,302 reflections measured ($5.906° \leq 2\Theta \leq 51.448°$), 670 unique (merging error $R_{int} = 0.0651$ and $R_{sigma} = 0.0137$) which were used in all calculations. The final structure confidence factor R_1 was 0.0453 ($I > 2\sigma(I)$) and the structure confidence factor wR_2 was 0.1284 (all data).

Computational details. Atomic coordinates were imported from the refined crystal structures. Only the hydrogen atoms in the frameworks were optimized as part of a periodic system by ab initio calculations. The optimizations were performed using the GGA PBE functional with Grimme's DFT-D dispersion correction, and the thresholds for geometry optimization and SCF convergence were chosen to be 2×10^{-6} eV. Single point energy calculations were performed using the GGA PBE functional with Grimme's DFT-D dispersion correction, and the threshold for SCF convergence was chosen to be 1×10^{-6} eV. Mulliken charges were calculated at the end of the SCF cycle. These atomic charges were used in all the molecular mechanics and molecular dynamics calculations.

Molecular mechanics and molecular dynamics simulations. All molecular mechanics and molecular dynamics calculations were performed using the Forcite-Plus module. Molecular dynamics simulations were performed using UFF with an Ewald summation method for both electrostatic and van der Waals interactions. An *NpT* ensemble was used at 298 K for 5 ns. The Nosé–Hoover–Langevin thermostat (Q_{ratio} of 0.1) and Andersen barostat (cell time constant of 5.0 ps) were used, with a 1 fs time step.

Potential energy scans for the FTR conformations and rotors. Potential energy scans were performed using the GAUSSIAN16 software available through the CINECA high performance computing centre[53].

FTR dicarboxylate conformation scans. The dicarboxylate conformation scans were performed using the MP2/6-311G(d) and MP2/6-311+G(d) levels of theory. Initial optimization for the dicarboxylate conformation scan was performed using the MP2/6-311G(d) level of theory with the rotor restrained in the crossed arrangement. Additional parameters for all calculations included an 'Ultrafine' integration grid, 'VeryTight' SCF convergence criteria with XQC algorithm and a 'Fine' optimization convergence. These methods were chosen since they work well for molecules with small changes in potential energies such as free-rotating methyl moieties[35,45,54]. The scans were performed by rotating the carboxylate groups of the FTR molecule from an angle of 90° (crossed) with respect to one another to an angle of 0° (in plane) with an increment of 2.5°. The rotor was optimized during the scan, making this a relaxed scan.

FTR rotor rotational scan. The potential energy surface scans for the FTR rotor were performed using the MP2/6-311G(d), MP2/6-311+G(d) (rigid and relaxed scans) and CCSD/6-311+G(d) (rigid scan) levels of theory. Additional parameters for all calculations included an 'Ultrafine' integration grid, 'VeryTight' SCF convergence criteria with XQC algorithm and a 'Fine' optimization convergence. Optimized geometries were used as input for the rotor potential energy scans. The rotors were scanned through 120° at 1.5° increments (through 60° at 5° increments for the CCSD method) following the symmetry of the FTR rotor moiety.

FTR rotor rotational scan using point charges. To evaluate the electrostatic contribution to the energy barrier of the rotator, potential energy surface

scans were performed on the bicyclo[1.1.1]pentane molecule (that is, the bicyclopentane–dicarboxylate ligand without the carboxylate moieties and capped off with hydrogen atoms). Point charges were placed at the positions of the oxygen atoms in the in-plane conformation. The point charges were assigned using ESP and NPA (NBO3) and the bicyclo[1.1.1]pentane rotor was then scanned relative to the plane of the point charges, like the scan for the full FTR dicarboxylate molecule. This scan yields an interaction energy that is purely electrostatic and aids in understanding the origin of the rotary barrier. The energy barrier for the crossed conformation results was found to be lower than 0.5 cal mol^{-1}.

Cross-polarization MAS ^{13}C NMR and ^{1}H T_1 solid-state NMR at 7 T. Solid-state ^{13}C NMR experiments were carried out with a Bruker Avance 300 instrument operating at a static field of 7.04 T, equipped with high-power amplifiers (1 kW) and a 4 mm double resonance MAS probe. Ramped-amplitude $^{13}C\{^{1}H\}$ cross-polarization experiments were performed at a spinning speed of 12.5 kHz, using a recycle delay of 5 s and a contact time of 2 ms. The proton 90° pulse was 2.9 µs. ^{13}C Single-pulse excitation ^{13}C experiments were run using a 90° pulse of 4.6 µs.

Quantitative solid-state ^{1}H single-pulse excitation MAS NMR spectra were performed with a Bruker Avance III 600 MHz instrument operating at 14.1 T, using a recycle delay of 20 s. A MAS Bruker probe head was used with 2.5 mm ZrO_2 rotors spinning at 30 kHz. The proton 90° pulse was 2.9 µs. The ^{1}H chemical shift was referenced to adamantane.

Measurements of ^{1}H T_1 were made at 300.13 MHz using the saturation recovery pulse sequence at a spinning speed of 8 kHz in the range of 200–298 K, with 32 scans for each recovery time. The proton 90° pulse was 3.65 µs. The stability and accuracy of the temperature controller (Bruker B-VT 2000) were both approximately 0.1 K.

The empty materials were characterized under both MAS and static conditions at 298 K and 163 K, after the activation at 403 K under vacuum overnight. A homemade apparatus was used for sealing the rotors in vacuum. Measurements of ^{1}H T_1 were performed in vials sealed in vacuum. The I_2@Zn-FTR sample was prepared by I_2 vapour adsorption at room temperature for 72 h.

Second moment calculation of dipolar interactions in static ^{1}H NMR spectra. The calculation of the second moment was performed using a homemade C++ version of the program proposed by Goc[41]. The program was optimized to manage large crystal cells and was able to distinguish between the contributions of intra- and inter-rotor interactions. The simulations were performed on a $3\times3\times3$ supercell, with $\varphi = 3°$ and $\theta = 15°$, and were repeated multiple times, especially for the lowest number of jumps, to obtain a better averaged value. The contribution of the intra-rotor interaction is higher than 98% for Zn-FTR and higher than 91% for Zr -FTR.

Profile simulation of multiple spin system of rotor in static ^{1}H NMR spectra. Zn-FTR showed a peculiar pattern in the static ^{1}H NMR spectra due to the dipolar coupling of the six hydrogens within the bicyclic rotator. The bicyclopentane exhibits a six spin-½ system for the hydrogens. The fitting was performed using a hydrogen nucleus distance of 1.92 Å, setting the hydrogens on the vertices of a hexagon with sides of 1.92 Å, as previously studied for the rotation of benzene intercalated in graphite layers[40].

Analysis of static ^{13}C NMR spectra. The static spectra were simulated with NMR-Weblab, assuming $\sigma_{xx} = 44$ ppm, $\sigma_{yy} = 60$ ppm and $\sigma_{zz} = 52$ ppm, with Euler angle α_0 and a cone angle of 90° (refs. [37,55,56]).

Solid-state NMR ^{1}H T_1 measurements at 1.66 T, 1 T and 0.66 T. We performed ^{1}H NMR measurements on the investigated Zn-FTR sample by means of a homemade set-up based on an Apollo spectrometer (TecMag). We generated static magnetic fields $0.66\,T \leq \mu 0H \leq 1.6\,T$ by means of an electromagnet (Bruker). The low-field ^{1}H T_1 measurements were performed on a Zn-FTR sample sealed in a glass tube under a 250 torr helium (HiQ Helium 6.0) atmosphere. We investigated the temperature window $4.2\,K \leq T \leq 300\,K$ by means of a flux cryostat (Oxford Instruments) with liquid nitrogen and liquid helium as cryogenic liquids, measuring the temperature locally by means of a thermocouple junction displaced from the sample by ~5 cm. Additionally, we accessed temperatures $1.3\,K \leq T \leq 4.2\,K$ by means of a static cryostat (International Cryogenics) by vapour pumping over a liquid helium bath. In these conditions, in addition to the thermocouple sensor, we kept control of the temperature by measuring the vapour pressure over the helium bath. We prepared an ad hoc resonant circuit composed of a coil (used to generate the alternating magnetic field and to detect the ^{1}H NMR signal inductively) and of external variable capacitors aimed at the optimization of the tuning/matching of the overall impedance at the working frequency. We tailored the coil specifically for the sample — which was sealed in a quartz tube under inert atmosphere to avoid deterioration by air contact—aiming to maximize its filling factor. We checked with both the empty quartz tube and the empty coil to ensure that the ^{1}H NMR signal was entirely originating from the protons within the investigated Zn-MOF sample. We quantified ^{1}H T_1 of the sample by means of the conventional inversion recovery radio frequency pulsed sequence. The relaxation times were fitted using the Kubo–Tomita equation[57].

Data availability

X-ray crystallographic data have been deposited at the Cambridge Crystallographic Data Centre (http://www.ccdc.cam.ac.uk/) with reference numbers CCDC 1994502 (single-crystal Zn-FTR), 1994503 (Zn-FTR refined from PXRD) and 1994504 (Zr-FTR refined from PXRD). A copy of the data can be obtained free of charge via https://www.ccdc.cam.ac.uk/structures/. All other data supporting the findings of this study are available within the article and its Supplementary Information. Data are also available from the corresponding author upon reasonable request. Raw data are available for Fig. 5. Source data are provided with this paper.

References

46. Coelho, A. A. Indexing of powder diffraction patterns by iterative use of singular value decomposition. *J. Appl. Cryst.* **36**, 86–95 (2003).
47. Coelho, A. A. & Kern, A. Discussion of the indexing algorithms within TOPAS. *CPD Newsletter* **32**, 43–45 (2005).
48. Macrae, C. F. et al. & . Mercury CSD 2.0 - new features for the vsualization and investigation of crystal structures. *J. Appl. Cryst.* **41**, 466–470 (2008).
49. Krause, L., Herbst-Irmer, R., Sheldrick, G. M. & Stalke, D. Comparison of silver and molybdenum microfocus X-ray sources for single-crystal structure determination. *J. Appl. Cryst* **48**, 3–10 (2015).
50. Dolomanov, O. V., Bourhis, L. J., Gildea, R. J., Howard, J. A. K. & Puschmann, H. OLEX2: A complete structure solution, refinement and analysis program. *J. Appl. Cryst* **42**, 339–341 (2009).
51. Sheldrick, G. M. A short history of *SHELX*. *Acta Cryst.* **A64**, 112–122 (2008).
52. Sheldrick, G. M. Crystal structure refinement with *SHELXL*. *Acta Cryst.* **C71**, 3–8 (2015).
53. Frisch, M. J. et al. Gaussian 16, Revision B.01 (Gaussian, 2016).
54. Zhao, Y., Mouhib, H., Li, G., Kleiner, I. & Stahl, W. Conformational analysis of tert-butyl acetate using a combination of microwave spectroscopy and quantum chemical calculations. *J. Mol. Spectrosc.* **322**, 38–42 (2016).
55. Macho, V., Brombacher, L. & Spiess, H. W. The NMR-WEBLAB: An internet approach to NMR lineshape analysis. *Appl. Magn. Reson.* **20**, 405–432 (2001).
56. Pecul, M., Dodziuk, H., Jaszunski, M., Lukin, O. & Leszezynski, J. Ab initio calculations of the NMR spectra of [1.1.1]propellane and bicyclo[1.1.1] pentane. *Phys. Chem. Chem. Phys.* **3**, 1986–1991 (1985).
57. Kubo, R. & Tomita, K. A general theory of magnetic resonance absorption. *J. Phys. Soc. Jpn* **9**, 888–919 (1954).

Acknowledgements

Financial support from the Italian Ministry of University and Research (MIUR) through the grant 'Dipartimenti di Eccellenza-2017 Materials For Energy' is acknowledged. This research was funded by the PRIN-2015CTEBBA-003 and PRIN-20173L7W8K grants. I. Supino is acknowledged for her help during sample preparation.

Author contributions

A.C. and P.S. conceived the study. J.P. designed the materials synthesis and characterization. S.B., G.P., M.N., and P.C. carried out the NMR measurements and C.B., the theoretical calculations. A.C., P.S. and S.B. wrote the manuscript with suggestions from all the authors.

Competing interests

The authors declare no competing interests.

Additional information

Supplementary information is available for this paper at https://doi.org/10.1038/s41557-020-0495-3.

Correspondence and requests for materials should be addressed to A.C. or P.S.

Reprints and permissions information is available at www.nature.com/reprints.